Spectroscopic comparisons of two different terrestrial basaltic environments: Exploring the correlation between nitrogen compounds and biomolecular signatures

D.M. Bower, A.C. Mcadam, C.S.C. Yang, Maeva Millan, R. Arevalo, C. Achilles, C. Knudson, T. Hewagama, C.A. Nixon, C.B. Fishman, et al.

Spectroscopic Comparisons of Two Different Terrestrial Basaltic Environments: exploring the correlation between nitrogen compounds and biomolecular signatures

D. M. Bower[1,2], A.C. McAdam[2], C.S.C. Yang[3], M. Millan[4,5], R. Arevalo Jr.[6], C. Achilles[1,2], C. Knudson[1,2], T. Hewagama[2], C. A. Nixon[2], C.B. Fishman[4], S.S. Johnson[4], Jacob Bleacher[2], Patrick Whelley[1,2]

[1]University of Maryland, Department of Astronomy, College Park, MD, 20742, dina.m.bower@nasa.gov,
[2]NASA/Goddard Space Flight Center, Greenbelt, MD 20771,
[3]Brimrose Technology Corp., Sparks-Glencoe, MD, 21152,
[4]Georgetown University, Washington, DC, 20057,
[55]Laboratoire Atmosphère, Observations Spatiales (LATMOS), LATMOS/IPSL, UVSQ Université Paris-Saclay, Sorbonne Université, CNRS, Guyancourt, France,
[6]University of Maryland, Department of Geology, College Park, MD, 20742

Abstract

Life detection in the solar system relies on the unambiguous identification of signatures of life and habitability. Organic molecules are essential to life as we know it, and yet many organic compounds are ubiquitous in the solar system and can be synthesized abiotically; thus, their presence alone is not indicative of life. On Earth, chemical signatures of life's processes are often left behind in minerals through the biologically induced formation of secondary minerals or intermediary organic complexes. In natural rocks biomolecules and organic species often co-occur with minerals, and their overlapping peaks can create difficulties in interpretation. In the process of identifying the minerals and organic species in our basaltic samples we noticed signatures for cyanates co-occurring with organic molecules. Cyanates are an overlooked group of nitrogen compounds in which C is bonded to N (e.g., OCN^- or SCN^-) that often co-occur with urea and ammonium in environments where microorganisms are present. These compounds are common in many terrestrial and oceanic environments and play an important role in biogeochemical nitrogen cycling. In natural systems, these compounds form as the result of multiple biogeochemical pathways, often from the interaction of microbes with a chemically active environment. These interactions leave behind signatures in the form biotic breakdown products such as urea or ammonium and organic reaction byproducts that are observable with spectroscopic methods. To explore these relationships, we used field-portable Raman spectrometers and laboratory micro-Raman imaging to characterize and compare samples collected from two different terrestrial basaltic environments, a lava tube on Mauna Loa, Hawaii, dominated by the precipitation of sulfate minerals and a geothermal stream at Hveragil, Iceland dominated by the precipitation of carbonate minerals. The Raman (RS) measurements were complemented by laser induced breakdown spectroscopy (LIBS), Long-wave Infrared (IR) LIBS, with the addition of gas chromatograph mass spectrometry (GC-MS) and inductively coupled plasma-mass spectrometry (ICP-MS) to identify cyanate compounds, biomolecules, and other nitrogenous compounds related to the breakdown or production of cyanate in host basalts and secondary precipitates. The RS data suggest that the reason for RS cyanate signatures in the carbonate samples could be due to luminescence artifacts while those detected in the host basalts may be due to hydrolysis chemistry. The cyanate signatures detected in the lava tube samples dominated by sulfates do not seem to be luminescence artifacts but may in fact be evidence of an active microbial nitrogen cycle. Our results inform the spectroscopic detection of cyanates in

planetary analog environments and the challenges in their identification. Further work is needed to understand their potential as biosignatures on other planetary bodies.

Introduction

Terrestrial volcanic regions are dynamic environments that continually shape the landscape. The lithologies and landforms in such settings provide a window into potentially habitable environments on ancient Mars or other rocky bodies where similar activity currently occurs or occurred in the past. These environments are of particular interest for planetary analog studies focused on astrobiology as they offer multiple niches for life to thrive. Lava tubes, for example, form in basaltic volcanic environments as the result of an initial lava flow that cools at the top while hot lava continues to flow below; the top layer solidifies, and the flowing layer drains out, leaving behind a long cave or tube beneath the surface [1, 2]. Over time, these basaltic rocks are permeated with meteoric water and colonized by various forms of life [3, 4]. Orbital observations of the Martian surface indicate the presence of lava tubes and other types of volcanic flow features. Lava tubes on Mars hold the potential for extant life as well as for the preservation of past life within a subsurface environment protected from harsh conditions or weathering at the surface [5]. In contrast, geothermal springs and streams are examples of surface volcanic environments in which large volumes of water interact with the volcanic system at depth before flowing through the surface rocks creating conditions amenable for life along the stream-rock interfaces. These environments may be analogous to ancient fluvial-volcanic environments on Mars, where potential signatures of life may be preserved with secondary mineral deposits [6, 7].

On Earth, signatures of life (biosignatures) include biofilms, microbial mats, and detectable biomolecules, as well as a variety of secondary minerals that form as a byproduct of metabolic activity and cation exchange between cellular components and mineral surfaces [8]. Ideally, more than one of these features can be detected together to eliminate any ambiguity in origin. One approach is to couple mineral and biomolecular signatures that indicate specific biotic processes. Cyanates are a group of nitrogen-bound compounds in which C is bonded to N (e.g., OCN^- or SCN^-) common in many terrestrial and oceanic biogeochemical systems [9, 10]. Cyanate forms biologically inside cells through the breakdown of urea and carbamoyl phosphate, which can then decompose to ammonium and CO_2. In oceanic systems cyanate is present in its ionic form and exhibits a “biological-like” vertical distribution and is produced via the degradation of organic material [10]. Cyanates also form abiotically in environments with fluid or aerosol cyanide sources and through photooxidation or chemical oxidation of cyanide, or decomposition of urea. In volcanically active environments, cyanate compounds form from the hydrolysis of volcanic cyanide (CN^-) or thiocyanate (SCN^-). Thiocyanates also form through abiotic chemical reactions with sulfide oxidation products in anoxic subaqueous sediments, linking cyanates to the sulfur cycle [11]. Cyanates in the environment coordinate with microbially scavenged metals from rocks forming metal-cyanates, and cyanates play a role in carbonate and sulfate formation in terrestrial volcanic systems [6, 12]. Since extant microbes are able to both produce and consume cyanates, and these interactions leave behind signatures in the form of secondary minerals and organic reaction byproducts, cyanates may be useful biosignatures.

Cyanates may also be useful for life detection beyond Earth due to their distinctive Raman spectra. Most compounds that are considered as potential biosignatures, such as microbial pigments, fatty acids, glycerols, esters, and membrane lipids are observed within the "fingerprint region" ~400 cm^{-1} – 1700 cm^{-1} and ~2800 cm^{-1} – 3000 cm^{-1} regions of the Raman spectrum [13, 14].The lower end of the Raman spectrum also includes signatures for minerals; multicomponent samples containing both organic materials and a mineral matrix often result in overlapping Raman signatures, complicating spectra. Sulfate and carbonate minerals in particular can be problematic in this regard, since characteristic sulfate peaks occur between ~ 975 – 1012 cm^{-1} and carbonate peaks occur between ~ 1080 – 1095 cm^{-1}, 1407 – 1445 cm^{-1}, and 1720 – 1760 cm^{-1} [15, 16]. These peak positions overlap with a suite of diagnostic biomolecular signatures, challenging interpretations of composition [17]. Raman signatures for cyanates are observed within the ~2000 cm^{-1} – 2300 cm^{-1} region of the spectrum thus avoiding such interferences . These prominant diagnostic Raman peaks for cyanates include: cyanate (-OCN) and cyanate ion (assym NCO stretch) ~2240 – 2260 cm^{-1} and 2100 – 2225 cm^{-1}, respectively; isocyanates (-N=C=O) ~2250 – 2300 cm^{-1}; isothiocyanates (-N=C=S) ~1900 – 2150 cm^{-1}; thiocyanates (-SC≡N) ~2135 – 2175 cm^{-1}; thiocyante ion (asym N=C=S str) ~2020 – 2190 [18].

In this study, we characterized samples of secondary mineral precipitates and the host basalts from two different terrestrial locations: Hveragil stream in the Kverkfjöll-Vatnajökull glacial region of Iceland and a lava tube on Mauna Loa, Hawaii (Fig. 1). The host lithologies of both locations are similar, dominated by tholeiitic basalts (e.g., composed mainly of Ca-plagioclase, forsterite, and pyroxene) in contact with water, and secondary mineral precipitates on their surfaces. Hveragil gorge, to the NE of Kverkfjöll, hosts a geothermal stream that cuts through the basaltic mountains of Kverkfjöll [19]. The warm (≥ 50°C) waters of Hveragil are CO_2-rich, with a neutral pH and high amounts of silica and chloride; the basalts are extensively coated with a carbonate rind (Fig. 1C) up to several cm in thickness [19, 20]. This site is exposed to volcanic aerosols and aerially transported ash, rain, and solar influx. The local and regional basalts also host a wide range of lichen communities. In contrast, the lava tube on Mauna Loa, Hawaii is partially isolated from surface processes. The host lava flows are located at ~2400 meters elevation. Beneath the surface, a network of lava tubes manifests a variety of features, such as corraloids, stalactites, veneers and powdery coatings, as well as visible colorations (green, pink, orange) often associated with microbial activity in other tube systems [4]. This sample site is located in a drier region relative to other locations on the island.

We used Raman spectroscopy (RS), complemented by a suite of geochemical techniques, such as UV-VIS-NIR + Long-wave IR laser induced breakdown spectroscopy (LIBS), and pyrolysis GC-MS to characterize the mineral, elemental, and organic composition of intact field samples as well as inductively coupled plasma mass spectrometry (ICP-MS) to quantify the abundances of alkali, alkaline earth, and transition metals in water samples collected from the same sites. The goal of this work is to inform the spectroscopic detection of cyanates in planetary analog environments and to understand their relationships with secondary minerals and organic molecules. Further laboratory studies will assess their potential as biosignatures.

Methods

Secondary precipitates and the host rocks were collected from both sites and kept in either a desiccation cabinet or cold storage in the laboratory. Sterile sampling techniques were used, including using ashed tools and sample jars with minimal sample handling using nitrile gloves.

The Hveragil samples included carbonate-encrusted basalts (Fig. 1A,B) that were collected from the water's edge. The samples from the Mauna Loa lava tube were collected from two main sections of the tube, one that was exposed to partial sunlight and a second section that was isolated from the surface and completely dark. Solid samples were collected throughout both sections of the tube (Fig. 1C,D)). In addition to the solid samples, liquid water samples were collected from two locations in the tube where water was actively seeping through the ceiling (Fig. 1E).

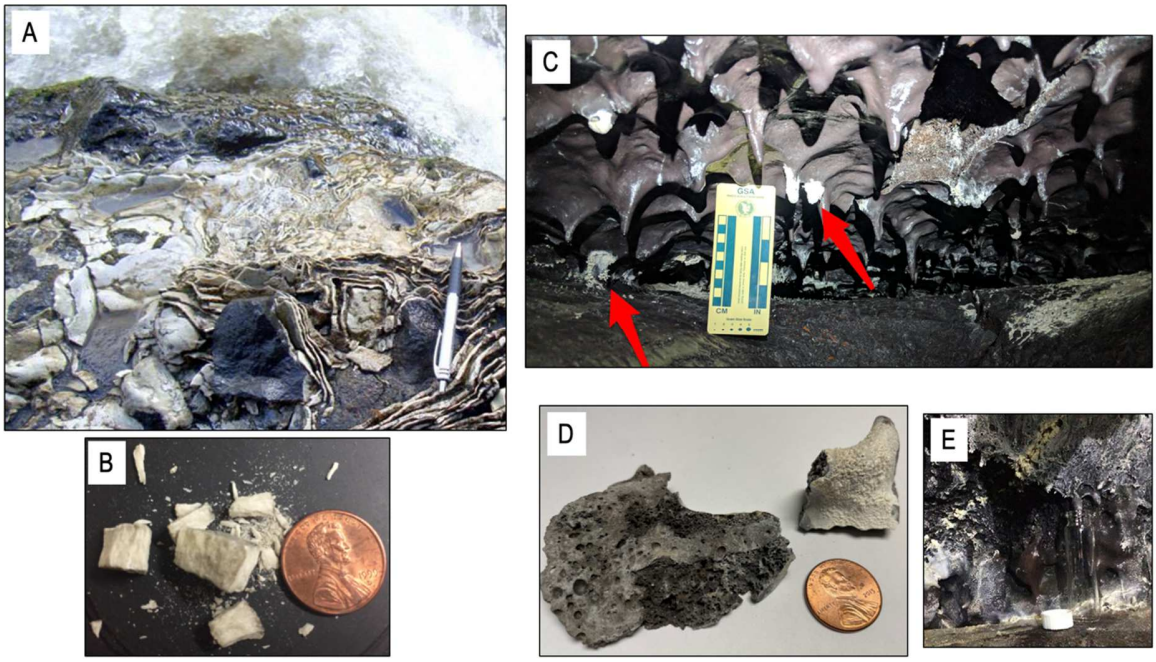

Figure 1. Field sites and representative examples of samples analyzed in this study. (A) Carbonate crusts coating basalts along the edge of Hveragil stream (pen for scale). (B) Fragments of carbonate rind collected and analyzed in the lab. (C) Brown veneer-coated mini-stalactites with sulfate crusts (upper arrow) and coralloids (lower arrow) in the Mauna Loa lava tube. (D) Fragments of the encrusted mini-stalactites collected and analyzed in the lab. (E) Cave water percolating from a coralloid collected in a glass vial.

We used a combination of field-portable Raman spectroscopy with micro-Raman spectroscopy and spectroscopic imaging to characterize the mineral assemblages, hydrated components, and biomolecules in secondary precipitates and host rocks collected from the Hveragil geothermal stream, Iceland and the lava tube on Mauna Loa, Hawaii (Fig. 1). In situ field measurements provided a way to observe real-time formation of cyanates in connection with newly formed minerals and extant microbial communities in the natural environment. Field measurements were done using a portable VIS Raman spectrometer (TSI, Inc. EZ Raman), which uses a 532 nm excitation laser with a 1.2 µm fiber optic probe and a spot size of 50 µm. Calcite ($CaCO_3$), gypsum ($CaSO_4 \cdot 2H_2O$), and quartz (SiO_2) minerals were used as calibration standards to keep track of any spectrometer drift and to accurately assign peak positions to our samples. The instrument has a spectral range between 100 to 4000 cm^{-1}, with a resolution of ~10 cm^{-1}. Power output is controlled by the software, and a minimum amount of power (0–3 - 2.0 mW) was applied as appropriate for each individual sample. Scan times varied for each sample, typically ~ 10-40 seconds/spot for each target. Returned samples were also probed in the laboratory using

the field-portable instrument with the same measurement parameters for additional data. Further laboratory Raman measurements were done with a WITec α-Scanning Near-Field Optical Microscope customized to incorporate confocal VIS (532 nm) Raman spectroscopy imaging utilizing 50x and 100x objectives to achieve a lateral resolution of ~300 nm and a spot size ~1 µm. Spectra maps and spot scans were done using low power at the sample (~0.05 – 3 mW) with acquisition times ~1-2 s/pixel for each map and 3-20 seconds/per spot for spot scans. A set of CN standards was measured to provide reference spectra (Fig. 2). These particular compounds were chosen because they exhibit the same type of coordination chemistry we might expect in natural volcanic systems where Fe, K, and Na are removed from basalts via weathering, which would be followed by CN-complexation to form stable insoluble metal-organo cyanates [21].

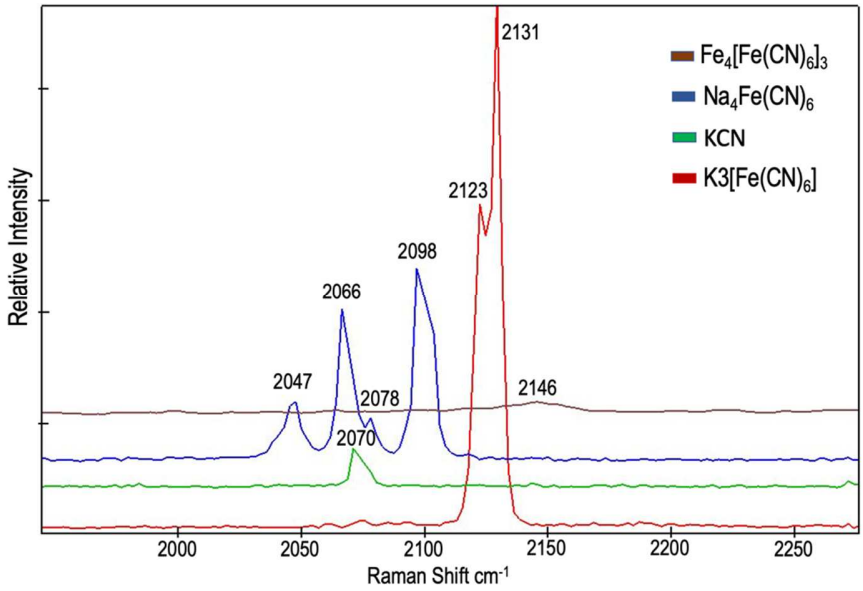

Figure 2. Reference spectra from CN powders taken with the WITec Raman system showing prominent CN peaks that are similar to what is present for the cyanate compounds observed in our field samples.

The Raman data collected with the portable instruments were processed using ACD labs Optical Workbench and Spectrus Processor software packages. Baseline correction and peak fitting was done manually using Gaussian – Lorentzian fits. For the micro-Raman imaging data, WITec Project Plus software was used to map peaks of interest across the sample, compute peak intensity maps, and for principle component analysis (PCA). Gaussian – Lorentzian fits were also used to baseline correct the spectra and to assign peaks. Interpretations of Raman spectra were based on careful comparisons to publicly available databases (e.g., RRUFF) and published literature (cited where relevant).

The Raman measurements were complemented by laboratory UV-VIS-NIR (UVN, 200 – 1000 nm) + Long-wave IR (LWIR, 5.6 to 10 µm, 1785 to 1000 cm^{-1} in the mid-IR region) laser induced breakdown spectroscopy (LIBS) to confirm the presence of the cyanates, discern cation variations in the secondary precipitates, and to identify a subset of the organic molecules. Simultaneous UVN + LWIR LIBS spectra were obtained by averaging results from four laser pulses sampling different spots on the sample surface. Calcite ($CaCO_3$), gypsum ($CaSO_4 \cdot$

197 $2H_2O$), quartz (SiO_2), magnetite (Fe_3O_4), alumina (Al_2O_3), feldspar and augite minerals, plus a
198 basalt from a GSI 1050-00E mounted specimen set, were used as calibration standards.
199 Fragments of the samples collected and returned from the field were mounted vertically on a xyz
200 translational sample stage that was positioned at 1 meter away from the front end of the
201 collection reflecting telescope and probed in the ambient atmosphere. Broad spectra of emission
202 signatures in both the UVN and LWIR spectral regions initiated by the same single laser-pulse-
203 induced micro-plasma on the target surface were recorded with a 3 µs delay with 10 µs
204 integration window for the UVN spectrometer and 24 µs delay with 44 µs integration window
205 for the LWIR spectrometer. From previous studies, we also estimated the possible detection limit
206 of simultaneous UVN + LWIR LIBS, to be in the range of 0.6-6 g/m^2 and 100-1000 ppm [22].

207 To further characterize the organic composition of the returned samples, pyrolysis GC-MS
208 experiments were conducted using a commercial Frontier Laboratories 3030D multi-shot
209 pyrolyzer (Quantum Analytics), and a trace 1310 GC coupled to a quadrupole mass spectrometer
210 (ThermoFisher) equipped with a Restek capillary MXT-5 column (30 m long x 0.25 mm ID
211 bonded with a 0.25 µm thick stationary phase). Prior to analysis, samples were powdered, and
212 aliquots (~10 mg) were deposited into the pyrolysis stainless-steel cup. The samples were first
213 flash-pyrolyzed at 200°C to remove the adsorbed water then analyzed using a slow ramp
214 temperature of 35 °C.min^{-1} at two ranges of temperature: 200-600°C, and 600-1050°C intended
215 to target the potential organics and/or biosignatures trapped in the carbonate and sulfate minerals
216 which decompose at higher temperature. During pyrolysis, volatilized molecules were trapped at
217 the column inlet using a liquid nitrogen cold trap (-180 °C); the GC injector downstream was set
218 between 250-300 °C to prevent the condensation. After pyrolysis, the cold trap was heated,
219 automatically triggering the beginning of the GC analysis. The temperature program used for the
220 GC was an initial temperature of 35 °C held for 5 min followed by a 5 °C.min^{-1} ramp up to a
221 final temperature of 300 °C held for 1 min to bake out the column prior to the next analysis.
222 Helium was used as the carrier gas and set at 1.2 ml.min^{-1} flow rate with a split flow of 10
223 ml.min^{-1}. The MS ion source and transfer line were both set at 300 °C and ions produced by the
224 70 eV electron ionization source were scanned with mass-to-charge ratios (*m/z*) between 40 and
225 535 with a scan time of 0.2 seconds. Flight-like wet chemistry experiments were also performed
226 with pyrolysis coupled with MTBSTFA-DMF derivatization, analogous to one of the wet
227 chemistry techniques currently utilized onboard the Sample Analysis at Mars (SAM) instrument
228 of the NASA Curiosity rover [23].

229 Inorganic cations in the water samples collected from the Mauna Loa lava tube were measured
230 quantitatively via ICP-MS to understand the potential role of pore water chemistry on the
231 composition of secondary precipitates and microbial processes. At the field site, glass vials were
232 positioned under actively dripping sites from the tube ceiling and left overnight to collect the
233 slowly percolating fluid (Fig.1E). In the laboratory, the water samples were filtered into–2 - 3 ml
234 volumes and spiked to 2 wt.% HNO_3. The samples, which were analyzed using a Thermo
235 Finnigan Element 2 single collector ICP-MS interfaced to an Apex high-sensitivity desolvating
236 nebulizer, were bracketed by five in-house calibration solutions composed of Na, Mg, Ca, Va,
237 Cr, Mn, Cu, As, and Ba spanning from 0.90 to 90 ppbw (also in 2 wt.% HNO_3). Thus, a
238 calibration curve was constructed to quantitate elemental abundances from observed count rates.
239 For reference, a blank consisting of only 2 wt.% HNO_3 was also analyzed along with the sample
240 set. All samples and standards were spiked with 1 ppbw to monitor for instrumental drift. Water
241 samples from Hveragil stream were not available for this study, so recently published water data
242 was used for those samples [19, 20].

Results

The analyses of our samples from both sites revealed interesting correlations of cyanates with biomolecules and mineralogy. The host basalts from both Iceland and Hawaii had similar compositions of plagioclase, pyroxene, and olivine minerals. The dominant secondary precipitates at Hveragil were carbonates; sulfates in the Mauna Loa lava tube. Similar biomolecular signatures were detected in samples from both Hveragil stream and the Mauna Loa lava tube, including pigments, organic acids, lipids, cyanates, and cyanate-related compounds. Table 1 outlines results from both sites based on the Raman and LIBS signatures of the main cyanate species and other co-occurring compounds that did not overlap with other biomolecular species on the lower end of the spectrum. The details for each location including potential peak overlaps are discussed individually below. The stream at Hveragil gorge and the Mauna Loa lava tube are open systems subject to both abiotic and biotic processes, so it is necessary to consider the potential inputs and outputs of cyanates and related compounds to each individual environment. Without metagenomic information to identify the communities and metabolisms present, it is not possible to discuss the direct biotic production of cyanates in these systems. We can, however, try to reconstruct the potential pathways involved in the microbial utilization of cyanates and their connection to secondary mineral precipitation.

Table 1. Cyanates and co-occurring species observed by Raman spectroscopy and LWIR LIBS in the Hveragil and Mauna Loa samples. B=basalt, P=precipitate, *Indicates slight shifts from listed Raman peak position that do not indicate a different species.

Raman Peaks (cm^{-1})	Species	Hveragil	Mauna Loa
2066	$Mn(CN)_6^{4-}$ or N=C=S Isothiocyanate	B, P	B, P*
2106	M-CN-N or S-C≡N Isothiocyanate	P	
2112	C=N	B	B, P
2170	-SC≡N Thiocyanate	B	B, P*
2246	O-C≡N Isocyanate	B	P
2270	O-C≡N Isocyanate	P	B, P*
2334	Nitrile		P
2404	P-H	P	P
2440	P-H	B	B, P
2460	P-H		P
2484	P-H	B,P	P
2605	OH/carboxylic acids	B	
2680	OH/carboxylic acids	B	
3050	CH	P	
3158	OH/carboxylic acid		P
3260	N-H	P	
3300	N-H		P*
3350	N-H	B	B*
3380	OH-NH		B
3400	OH-NH	P	
3480	OH-NH	P	

Table 2. Signatures observed by LWIR LIBS in the Hveragil and Mauna Loa samples that correspond to cyanate compounds. B=basalt, P=precipitate.

LWIR LIBS Peaks (μm)	Species	Hveragil	Mauna Loa
9.53-9.56	C=N	B,P	B,P
9.35	C=N	B,P	B,P
9.05	S-C≡N	B,P	B,P
8.96	C=N	B	
8.57	C=N		B,P
6.98	O-C≡N	B	B,P
6.55	N-H		B,P
6.23	C=N		P

Hveragil Stream, Iceland

The basalts at Hveragil were mainly composed of plagioclase minerals anorthite ($CaAl_2Si_2O_8$) based on Raman peaks 404 cm^{-1}, 507 cm^{-1}, 560 cm^{-1}, 625 cm^{-1}, and 797 cm^{-1}, and oligoclase $(Na,Ca)(Si,Al)_4O_8$ based on peaks 142 cm^{-1}, 287 cm^{-1}, 450 cm^{-1}, 478 cm^{-1}, 508 cm^{-1}, 790 cm^{-1}, 996 cm^{-1}. Transitions between pyroxene minerals diopside ($CaMgSi_2O_6$) and wollastonite ($CaSiO_3$) were also evident by peaks ~ 160 cm^{-1}, 302 cm^{-1}, 324 cm^{-1}, 414 cm^{-1}, 488 cm^{-1}, 888 cm^{-1}, 960 $cm^{-1}$and 1018 cm^{-1} [24]. The UVN LIBS spectra were dominated by atomic emissions for the major cations that make up the minerals detected by Raman: Ca, Na, Mg, Al, with other components Ti, K, and Fe common for typical basaltic minerals. The LWIR LIBS spectra also showed intense O-Si and O-Al stretching features of the $(Si,Al)_4O_8$ structure of the plagioclase minerals between 8.6-9.7 μm (11–9 - 1030 cm^{-1}) (Fig. 3C).

Biomolecules detected on the basalts with Raman spectroscopy included a wide variety of different types of organic acids, pigments, and cyanates with pyroxene and/or plagioclase, reflecting the diversity of communities colonizing the basalts. Amino acids were identified based on peaks (C-C) 952 cm^{-1}, (NH) 1556 cm^{-1}, (CO) 1670 cm^{-1}, (C=O) 1826 cm^{-1}, and (NH) 3240 cm^{-1}. Carotenoids are also observed with Raman peaks 1006 cm^{-1}, 1148 cm^{-1}, and 1519 cm^{-1}, and parietin ($C_{16}H_{12}O_5$) by peaks 590 cm^{-1}, 613 cm^{-1}, 718 cm^{-1}, 1118 cm^{-1}, 1178 cm^{-1}, 1552 cm^{-1}, and 1621 cm^{-1}. Atranorin ($C_{19}H_{18}O_8$), an anthraquinone compound associated with lichens, was also frequently observed by peaks 588 cm^{-1}, 1254 cm^{-1}, 1642 cm^{-1}, and 1670 cm^{-1}[25].

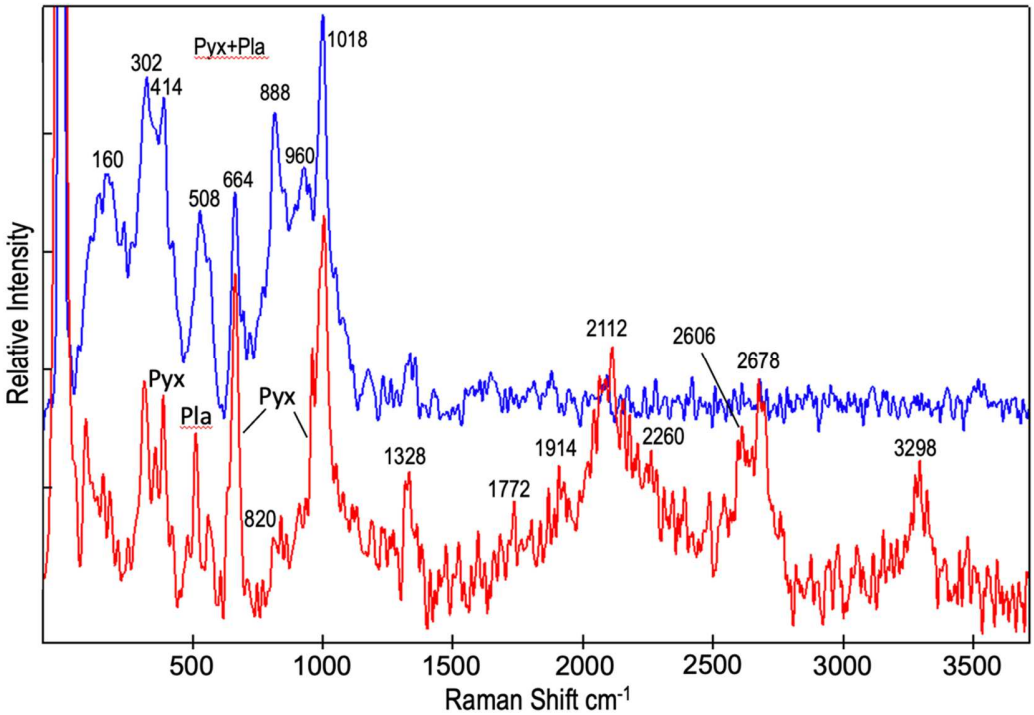

Figure 3. Raman spectra collected from a sample of Hveragil basalt using the micro-Raman spectrometer shows presence of cyanates with pyroxene in some areas and none in others. Spot one (Blue) shows pyroxene (Pyx) and plagioclase (Pla) spectrum without cyanate peaks, while spot two (Red) shows pyroxene-plagioclase (160 cm^{-1}, 302 cm^{-1}, 414 cm^{-1}, 508 cm^{-1}, 664 cm^{-1}, 888 cm^{-1}, 960 cm^{-1}, 1018 cm^{-1} with cyanates 2112 cm^{-1} and 2260 cm^{-1}), organic molecules (1328 cm^{-1}, 1772 cm^{-1}, 1914 cm^{-1}), carboxyl-OH groups (2606 cm^{-1}, 2678 cm^{-1}, and 3298 cm^{-1}), and Si-C peak (820 cm^{-1}).

Raman signatures for cyanates were observed by recurring peaks (M-CN or isocyanate) 2066 cm^{-1}, (C=N) 2112 cm^{-1}, (M-CN) 2168 cm^{-1}, and (O–N - isocyanate) 2246 cm^{-1}, with (P-H) 2444 cm^{-1} (Table 1). Peak shifts in the pyroxene spectra ~323 cm^{-1}, 388 cm^{-1}, 530 cm^{-1}, 664 cm^{-1}, 930 cm^{-1}, 999 cm^{-1} combined with biomolecular peaks (CH_2) 1328 cm^{-1}, (C=O) 1772 cm^{-1}, (C=C=C) 1914 cm^{-1}, and cyanate peaks 2112 cm^{-1}, 2262 cm^{-1}, carboxyl peak 2606 cm^{-1}, (OH) 2678 cm^{-1}, (C-H) 3298 cm^{-1}, and (Si-C stretch) 820 cm^{-1} may indicate biomolecular coordination within the pyroxene lattice and/or adsorption to the surface (Fig. 3) [18]. In addition, a Raman peak centered at 1292 cm^{-1} was also frequently observed with the cyanates, which could be attributed to either NCO^- or a methyl-silicon coordination [18]. An additional Si-H band ~950 cm^{-1} was observed with this peak. Raman peaks ~888 cm^{-1}, 996 cm^{-1}, 1018 cm^{-1}, and 1044 cm^{-1} indicative of urea were observed sporadically in the basalt samples along with peaks ~2444 cm^{-1} (PH_2) and ~950 cm^{-1} (PH), but the overlap with some of the pyroxene and plagioclase peaks makes a definitive identification difficult [12, 26].

The LWIR LIBS detected CH deformation bands of organic acids, amino acids and neutral chlorophyll at 6.74, 6.78, and 7.12 µm (1483, 1474, and 1404 cm^{-1}) in the Hveragil basalt samples. Figure 4C shows he C–O stretching bands of amino acids at 9.44 µm (1059 cm^{-1}) and 9.83 µm (1017 cm^{-1}) and the CN stretching bands attributed to either amino acid, chlorophyll or

cyanates at 8.96 µm, 9.35 µm, and 9.53 µm (1112, 1069, and 1049 cm^{-1})[27-29] The emission signatures of isocyanates (OCN) and thiocyanate (SCN) were observed at 6.98 (1433 cm^{-1}) and 9.05 (1105 cm^{-1}) µm respectively [30, 31]. Water was also detected in the basalt samples by the occurrence of the LWIR LIBS 6.6-6.8 µm (1470-1515 cm^{-1}) water bending band along with weak water bands in the 6.45 to 8 µm (1250-1550 cm^{-1}) region. The K identified with UVN LIBS at 766 nm and 769 nm could indicate the presence of a potassium feldspar or phyllosilicate. Neither potassium feldspars nor hydrated minerals were not detected in the basalts with the Raman measurements. Potassium feldspars are typically distinguishable from other types of plagioclase minerals with Raman spectroscopy, and a previous study on other lavas and volcanic sediments in the area near Hveragil did not detect K-feldspar, but did detect hydrated silicates [6]. The combination of water, K, and prevalence of Al in the LIBS spectra more likely indicates a phyllosilicate, and it is possible that the typically weaker Raman signatures for phyllosilicates were lost among the other components present in the basalt samples [32].

The carbonate rind is characterized by Raman spectra containing a mix of different carbonates dominated mostly by calcite ($CaCO_3$) based on peaks ~ 154 cm^{-1}, 278 cm^{-1}, 712 cm^{-1}, 1084 cm^{-1}. Variations in Raman peak positions in many of the samples ~702-712 cm^{-1} (calcite), 1097 cm^{-1} (magnesite), and 1437 cm^{-1} (calcite) suggested solid-solution transitions [33]. The LIBS data confirmed these variations and helped to clarify any other possible cation assignments suggested by the Raman spectra. The UVN LIBS spectra were dominated by intense atomic emissions of Ca (393 nm, 397 nm, 443 nm, 445 nm, 504 nm, 558 nm, 585 nm, 617 nm and 646 nm), with observable emission features of Mg (384 nm, 517 nm) and Mn at (403 nm, 476 nm, 478 nm, and 482 nm) (Fig. 4D). The LWIR LIBS spectrum was dominated by a strong CO_3 antisymmetric stretching vibrational feature at 6.8 µm (1470 cm^{-1}) [34]. Typical LIBS emission features of basalt samples such as atomic signatures of Fe, Ti in the visible and molecular signatures of O-Si-O, O-Al-O in the infrared were absent in the UVN + LWIR LIBS spectra of carbonate samples. Signatures for organic acids and oxalates typically associated with lichens were identified in the carbonates by peaks ~ 1277 cm^{-1}, 1466 cm^{-1}, 1592 cm^{-1}, and 1668 cm^{-} [17, 35, 36]. Recurring Raman peak sequences likely indicative of ketones were detected by (C-O-C) 1207 cm^{-1}, (C-H) 1405 cm^{-1}, (C-CH)1619 cm^{-1}, (C=O)1643 cm^{-1}, (ν C=O) 1762 cm^{-1}. The C=C stretching mode at 1502 cm^{-1} typically ascribed to carotenoids was also observed in the samples, but the other representative bands for these compounds were absent or obscured by other signatures [17].

Potential Raman signatures for cyanates ~ (M-CN) 2062 cm^{-1}, (C=N) 2106 cm^{-1}, (SCN) 2196 cm^{-1}, (C≡N) 2270 cm^{-1}occurred with recurring biomolecular signatures (C-O-C) 934 cm^{-1}, (-COOH) 1356 cm^{-1}, (COO^{-}) 1562 cm^{-1}, (ν C=C) 1658 cm^{-1}, (C=O) 1778 cm^{-1}, and (C=O) 1801 cm^{-1} with the addition of (P-H) 2408 cm^{-1}, (CH) 2484 cm^{-1}, (carboxyl OH) 2530 cm^{-1}, (CH_3) 3056 cm^{-1}, (C-H) 3130 cm^{-1}, (OH) 3142 cm^{-1}, (O-H) 3262 cm^{-1}, (NH_2) 3372 cm^{-1}, (O-H) 3402 cm^{-1}, (CH_2SH) 2672 cm^{-1}, (N-H) 3478 cm^{-1}, and (-OH, free carboxylic acid) 3562 cm^{-1} [18, 37]. No signatures for urea were observed in the carbonates. Carbamate (H_2NCONH_2) was only sporadically detected by peaks ~1694 cm^{-1} in both the carbonate and basalt. Other carbamate peaks ~563 cm^{-1} and 1405 cm^{-1} that would have helped in our interpretation overlap with mineral and biomolecular signatures and were not readily observed in our samples. Methyl groups were also identified in association with lipids signatures in the same spectra with the cyanates with peaks ~2760 cm^{-1}, 2870 cm^{-1}, 2930 cm^{-1}, and 3030 cm^{-1} [13].

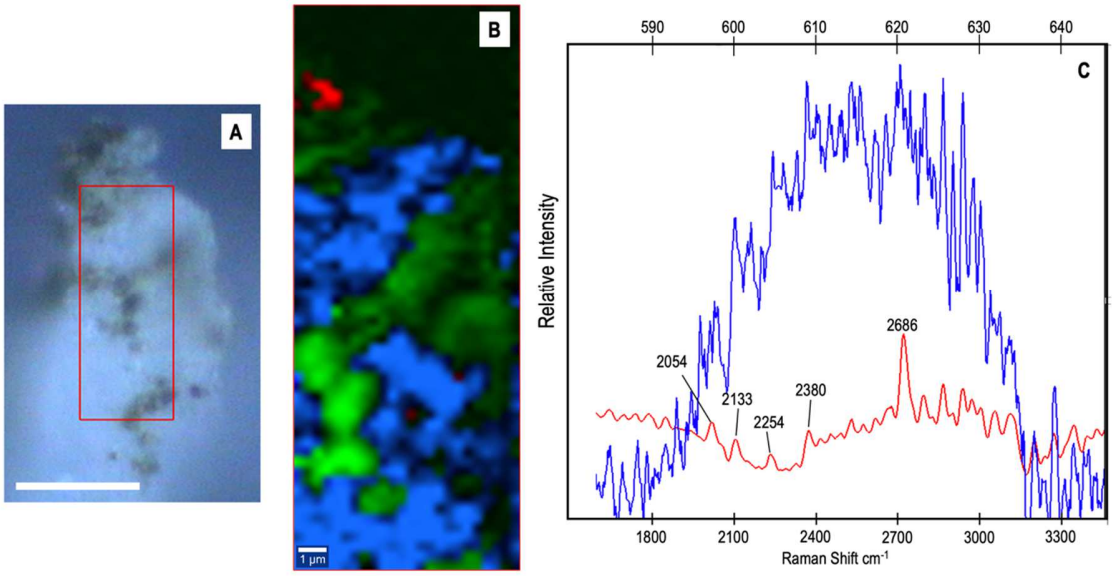

Figure 4. Micro-Raman analysis of carbonate sample from Iceland shows Mn-oxide mineral and either potential evidence of cyanates or artifacts of luminescence. (A) Image of the sample surface through the microscope, red box shows 8 μm x 20 μm scan area, scale = 10 μm. (B) Raman map showing mix of Mn-oxide (green) and potential cyanates (red) in the Ca-carbonate (blue). (C) Raman spectra from map in (B) showing cyanates or luminescence (blue spectrum) and isolated cyanate + carboxylic acids spectrum (red). Upper axis shows luminescent peak positions in nm, lower axis Raman shift. Note the lack of peak position specificity except for the OH-carboxyl group at 2686 cm^{-1}, other peaks are "in the range" of typical cyanates.

The carbonate rind also contained precipitates of Mn-oxide as identified by Raman peaks ~196 cm^{-1}, 258 cm^{-1}, 389 cm^{-1}, 541 cm^{-1}, 569 cm^{-1}, 620 cm^{-1}, 656 cm^{-1}, and in some cases 3345 cm^{-1} indicating some hydrated phases. Mn-oxides are known to occur with carbonates in general, and are often associated with young and unaltered lavas and basalts on Iceland [38, 39]. Evidence of Mn-cyanate complexes occurs as Raman peaks (Mn $(CN)_6^{-4}$) 2062 cm^{-1} and (Mn-CN-Mn) 2106 cm^{-1} in some areas of the carbonates as well. The cyanate peaks in this case could also correlate with luminescence features common to carbonates, phosphates, rare Earth elements (REE's), and metals such as Mn^{2+} under 532 nm laser excitation [40, 41]. The bands we attribute to cyanates and phosphor compounds in our samples occur at 597 nm, 600 nm, 604 nm, 608, nm, and 620 nm, which are similar to bands that have been observed for carbonate-hosted apatite [38]. We did not detect any phosphate minerals and could not confirm the presence of REE's within the scope of the study. Coordination between the calcite and Mn^{2+} may be contributing to these features, and other studies suggest that this is often in combination with REE's. In some cases, subtraction of the luminescence background resulted in weak-medium peaks that could be assigned to cyanates and carboxyl groups, but we can't rule out the potential effect of the Mn in these carbonate samples (Fig. 4). Further work will be done to better understand the overlap among these features.

The presence of Mn in the carbonate was also confirmed by the LIBS measurements (Fig. 5). Strong atomic emission signatures of Mn at 403, 476, 478, and 482 nm could be identified in UVN LIBS spectra of the carbonate samples. Some signatures indicative of cyanates were also observed by the LWIR LIBS measurements with the keto C=O stretching band of chlorophyll derivatives at 5.9 µm (1694 cm^{-1}) along with C-N stretching bands at 9.35 and 9.53 µm (1069 and 1049 cm^{-1}) [28]. A few weak vibrational bands of amino acids were observed as well: CH bending at 9.23 µm (1083 cm^{-1}), C-O stretching at 9.44 µm (1059 cm^{-1}) and C-C stretching at 9.86 µm (1014 cm^{-1}) [29]. In addition, a weak feature of thiocyanate (SCN) could be seen 9.05 µm (1105 cm^{-1}) in some of the spectra. Thiocyanate was detected in the basalts with Raman spectroscopy, but not in the carbonates.

Thiocyanates naturally form in the environment through the microbial conversion of cyanide or the breakdown of plant-based compounds like glucosinolate ($C_7H_{11}NO_9S_2$-R) [42]. Neither cyanide or glucosinolate were identified in our samples, but with the variety of plant life in the area, it is possible that plants could be contributing to this signal. Instead of thiocyanates, the potential Mn-complexing with the cyanates is suggested by overlapping Raman peaks ($Mn(CN)_6^{-4}$) 2062 cm^{-1} and (Mn-CN-Mn) 2106 cm^{-1}, and is confirmed by the LIBS data. Based on other studies of the region, Mn is not known to be a constituent of the stream water, but we detected it in the basalts [19]. The Mn in the oxides and carbonates in these samples could have been weathered from pyroxenes, olivines, or Mn-filled microfractures in the host basalts through exposure by the vigorous geothermal stream regime at Hveragil or by microbial scavenging, as evidenced by the prevalence of biomolecular signatures in these samples [39] [43, 44]. This could be an additional pathway involving mineral precipitation via both abiotic and biotic processes. This will be explored further with thin section analyses where these process-driven associations can be revealed in higher detail [45, 46].

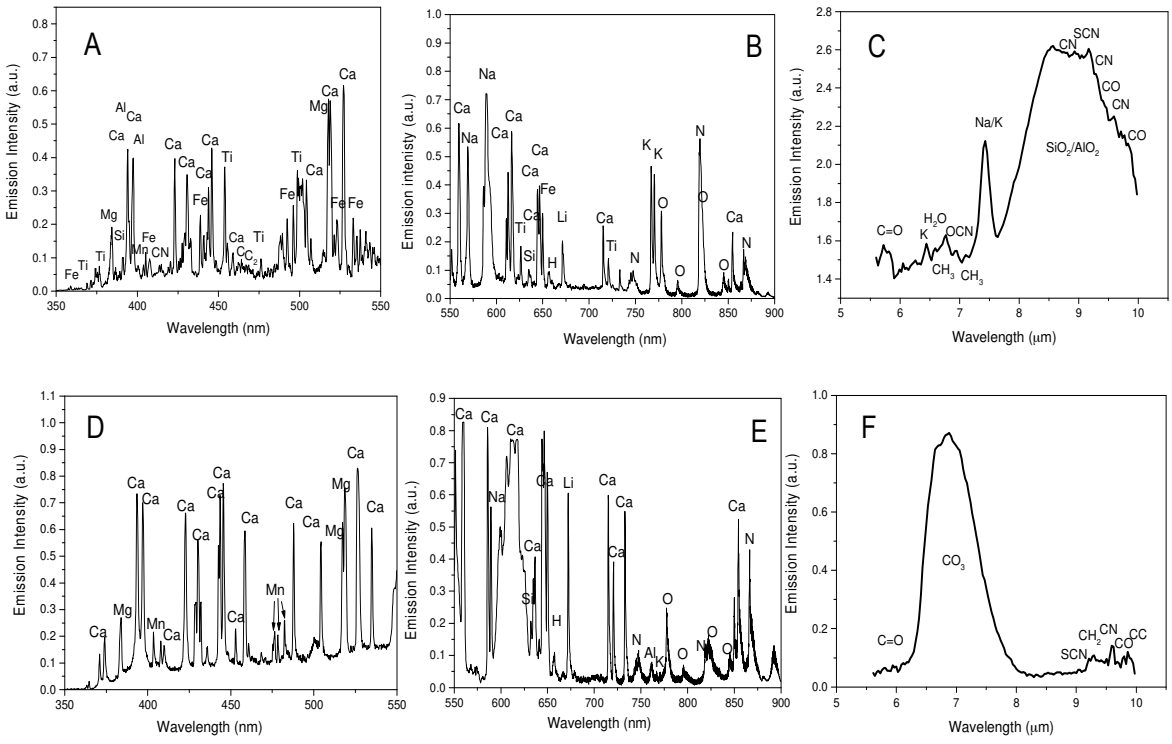

Figure 5. LIBS spectra from Hveragil basalt and carbonate confirm Raman compositional information and also reveal the presence of mineral phases not detected with Raman. (A,B) UVN LIBS spectra shows elemental composition indicative of plagioclase and a K-rich mineral (C) LWIR LIBS spectrum showing vibrational emission features of amino acids, chlorophyll, plagioclase, and possibly cyanates. (D-E) UVN LIBS of the carbonate shows a mix of cations (Ca, Mg, Mn) are present within the carbonate mineral structure along with N. (F) LWIR LIBS showing carbonate band with biomolecular signatures and potential signatures for cyanates.

Microbial mats, lichen communities, and mosses all co-colonize the basalts along the edge of Hveragil stream, providing a consortium of potential cyanate producers and consumers. The recurring combination of cyanates and biomolecules is intriguing. In the context of cyanate chemistry, the microbial colonization of the carbonates certainly could have occurred following their precipitation on the basalts, linking the formation of carbonate minerals mainly with hydrolysis chemistry [12]. In this type of system, the hydrolysis of the cyanate ion results in the formation of carbonate and ammonium: $OCN^- + 2H_2O \rightarrow CO_3 + NH_4$. Given that the region of Hveragil is volcanically active, the source of OCN^- could be magmatic in origin, though data from direct measurements of CN species in this region is not well known [19]. OCN^- was not detected in the basalt or carbonates with Raman or LIBS, which could be attributed either to the reaction going to completion or a lack of homogeneity in the samples. In addition to the carbonate being produced, we would expect to detect ammonium based on this pathway, but any potential ammonium peaks would have overlapped with other peaks we observed with the cyanates, such as ~3260 cm^{-1} (CH) and 3349 cm^{-1} (NH_2), though organic nitrite compounds can exhibit N=O overtones –3220 - 3360. The microbial uptake of the NH_4 in this case could have resulted in the conversion to nitrate or nitrite. The other dominant lower frequency Raman peaks for nitrate ~1615 - 1650 cm^{-1} and nitrite ~1610 - 1625 cm^{-1}, respectively overlap with peaks for other biomolecules we identified (e.g., ketones), again complicating our interpretation.

Urea (H_2NCOO^-) and carbamate (H_2NCONH_2) are also formed during the hydrolysis of OCN^- to carbonate: $3OCN^{-1} + 3H_2O \rightarrow H_2NCOO^- + H_2NCONH_2 + CO_3^{-2}$ [12]. Urea was detected in the basalt, but not the carbonate, and carbamate was weakly identified in both the carbonate and basalt. The lack of urea in the carbonate could be due to microbial consumption of the urea from the surface of the basalts as the carbonates are formed. Some studies have shown that the microbial breakdown of urea enhances calcite precipitation under similar conditions, with a release of ammonium into the system [47, 48]. This may also partially explain why we did not definitively detect ammonium peaks in our samples. Byproducts of carbamate metabolism include methylamines and dihydroxy aromatic intermediates [49]. We did observe recurring Raman peaks indicative of general amine groups in the carbonate at ~3449 cm^{-1}, but not in the basalt.

The GC-MS data indicated the presence of a variety of numerous organic molecules, however no cyanates, urea, or specific byproducts were detected. The flash-pyrolysis at 200°C allowed the release most of the water and showed the presence of CO_2. The chromatograms obtained after the 200-600°C pyrolysis temperature range showed the presence of more than 200 molecules including mainly oxygen-, and nitrogen-bearing aliphatic and aromatic compounds, saturated and

unsaturated hydrocarbons, and mono-, and polycyclic aromatic hydrocarbons up to three carbon rings (Fig. 6). The nitrogen-bearing species represented about 10% of the total number of compounds detected and included mostly nitriles and aromatics such as pyrroles, and pyridines. More specifically, C_6-C_{27} *n*-alkanes were detected together with C_6-C_{19} *n*-alkenes isomers. The chromatograms obtained after the 600-1050°C pyrolysis temperature range revealed the presence of far fewer compounds (~10) and included SO_2, nitrogen-bearing aliphatic molecules (acetonitrile and propanenitrile), a few aromatics (benzene, toluene, and phenanthrene), and C_{13}, C_{15}, and C_{17} *n*-alkanes.

The presence of alkanes-alkenes doublets together with aromatic compounds is the typical signature obtained after the pyrolysis GC-MS of terrestrial biological kerogen [50]. These alkanes-alkenes pairs may originate from the defunctionalization of lipids such as fatty acids and alcohols, which undergo decarbonylation and decarboxylation reactions during diagenesis. Pyrolysis can introduce a bias regarding this hypothesis since it also induces the decarboxylation of the fatty acids potentially present in the sample. The results obtained after pyrolysis coupled with MTBSTFA-DMF derivatization only revealed the presence of a few (di)carboxylic and fatty acids including derivatized propanoic acid, levulinic acid, nonanoic acid, and a derivatized alcohol (dodecanol). Long-chain alkanes were still present in the chromatogram obtained after derivatization of Hveragil indicating that at least a portion of those were native to the sample and not entirely resulting from the decarboxylation of fatty acids during pyrolysis. Both the Raman and LIBS data confirm the presence of fatty acids and carboxyl groups occurring with the cyanate signatures in the samples, suggesting a relationship between them. Wet chemistry experiments that help the extraction, separation, and detection of fatty acids will be done in the future to clarify the alkane-alkene pair sources.

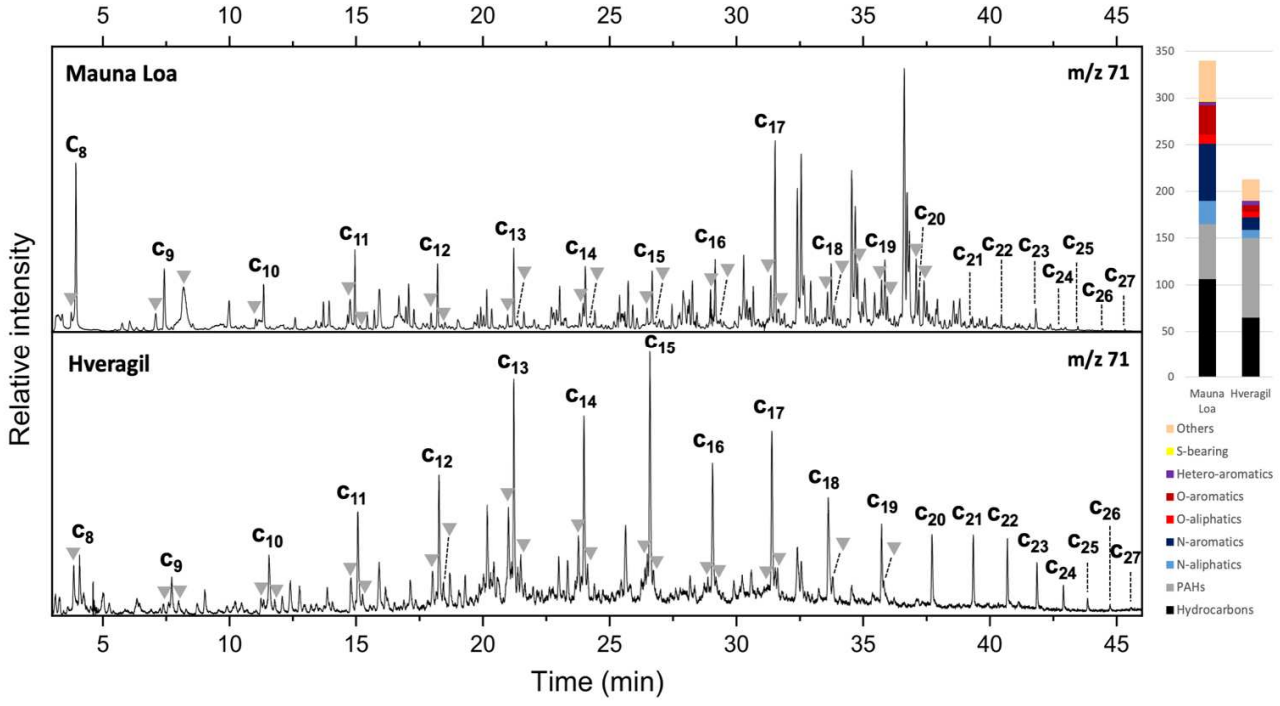

Figure 6. Portion of the extracted m/z 71 ion chromatograms obtained from the 200-600°C pyrolysis of one of the Mauna Loa (top) and Hveragil (bottom) samples displaying the detection of C_8-C_{27} n-alkanes and C_8-C_{20} alkenes represented with gray triangles. The histograms (right) show the total number of compounds detected and their chemical families of the representative Mauna Loa sample (340 compounds) and Hveragil (214 compounds). Chemical families include from bottom to top: hydrocarbons (black), polycyclic aromatic hydrocarbon (gray), nitrogen-bearing aliphatic and aromatic compound (light and dark blue, respectively), oxygen-bearing aliphatic and aromatic compounds (light and dark red, respectively), hetero-aromatics which represent aromatic compound containing several main atoms (purple), sulfur-bearing compounds (yellow), and "others" (pink) which represent the molecules that did not belong to the other categories and those that were not identified.

Lava Tube on Mauna Loa, Hawaii

The host basalts in the lava tube are composed of plagioclase, pyroxene, olivine, and hematite. The pyroxenes in the basalts exhibit solid solution polytypes based on variations in Ca, Mg, or Fe (enstatite-diopside-augite) with Raman peaks ~320 cm^{-1}, 350 cm^{-1}, 370 cm^{-1}, 416 cm^{-1}, 660 cm^{-1}, 670 cm^{-1}, 947 cm^{-1}, 990 cm^{-1}, 1012 cm^{-1}, and 1048 cm^{-1}. Ca-plagioclase (anorthite) was identified by Raman peaks ~ 404 cm^{-1}, 507 cm^{-1}, 560 cm^{-1}, 625 cm^{-1}, and 797 cm^{-1} with Na-plagioclase (albite-oligoclase) by Raman peaks ~180 cm^{-1}, 290 cm^{-1}, 486 cm^{-1}, 510 cm^{-1}, and 765 cm^{-1}. Signatures for cyanates in host basalts were rare and mostly detected in hematite-rich portions underneath the rinds. These cyanates were observed in association with organic acids at ~908 cm^{-1}, 1030 cm^{-1}, 1248 cm^{-1}, 1319 cm^{-1}, 1384 cm^{-1}, 1609 $cm^{-1}$and amino acids at ~848 cm^{-1}, 1168 cm^{-1}, and 1508 cm^{-1}. Fatty acids including sterols were also detected by peaks ~547 cm^{-1}, 1130 cm^{-1}, 1460cm^{-1}, 1660 cm^{-1}, 2860 cm^{-1}, and 2933 cm^{-1}.

In many areas of our lava tube, the secondary precipitates formed on the surfaces or along cracks of basaltic rinds or veneers. These rinds form at high temperatures and out-gassing as the lava drains from the tube during formation, and they are typically composed of lava oxidation products, such as iron oxides, oxyhydrides, and silicate glasses [51]. The veneers coating the basalts in the lava tube varied in color from dark brown, red, orange, and mustard yellow with compositions of mixed iron oxides. Biomolecular signatures were only rarely observed on the outer veneer surfaces, but freshly excavated granular material underneath the veneers contained such signatures along with those of plagioclase, pyroxene, olivine, and hematite.

The secondary precipitates in the lava tube were dominated by sulfates, minor carbonates, and hydrated silicates. Gypsum ($CaSO_4 \cdot 2H_2O$) was identified by recurring Raman peaks (+/- 5 cm^{-1}) at ~416 cm^{-1}, 480 cm^{-1}, 618 cm^{-1}, 670 cm^{-1}, 1012 cm^{-1}, 1136 cm^{-1}, 3390 cm^{-1}, and 3494 cm^{-1} in the majority of samples collected throughout the tube (Fig. 7). Thenardite ($NaSO_4$) was the second most common secondary precipitate, identified by recurring Raman peaks at ~ 452 cm^{-1}, 467 cm^{-1}, 622 cm^{-1}, 634 cm^{-1}, 649 cm^{-1}, 995 cm^{-1}, 1104 cm^{-1}, 1133 cm^{-1}, 1154 cm^{-1}. In the first part of the tube the thenardite occurred sporadically as a minor component of the secondary precipitates, and it was the dominant sulfate in the more isolated part of the tube. Minor potassium-thenardite was also identified with the thenardite by peaks at 998 cm^{-1}, 1078 cm^{-1}, 1133 cm^{-1}, and 1201 cm^{-1} [16, 52]. The minor carbonates were composed of calcite ($CaCO_3$), based on peaks at 284 cm^{-1}, 1087 cm^{-1}, 1758 cm^{-1}.

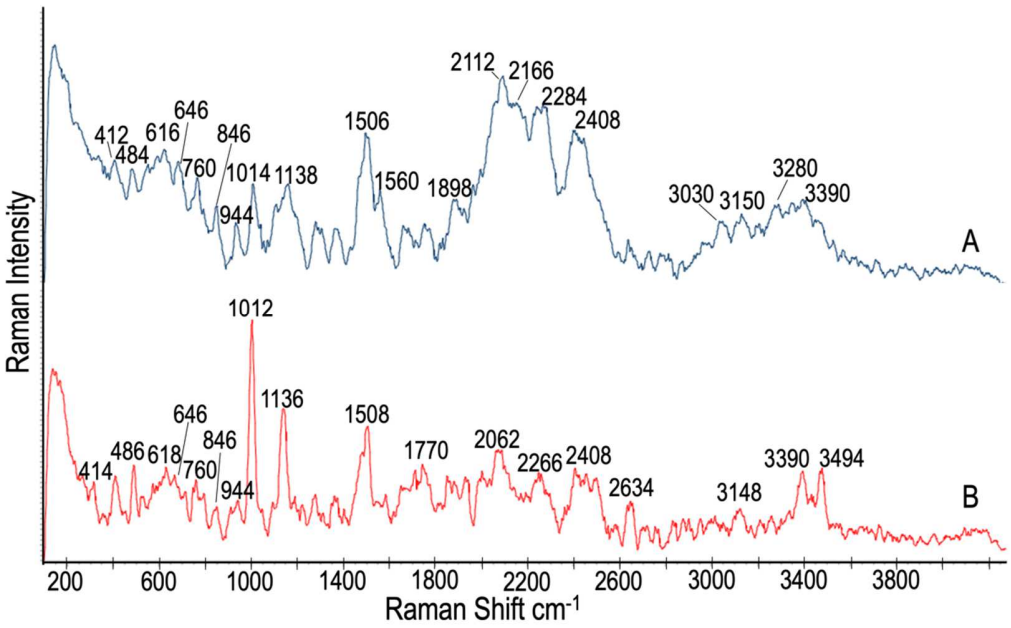

Figure 7. Raman spectra collected in situ with the field portable instrument from two different deposits in the Mauna Loa lava tube showing gypsum composition with organic molecules and cyanate compounds. (A) Spectrum from a white crust that formed on a lower wall of the lava tube with peaks for gypsum (412 cm^{-1}, 484 cm^{-1}, 616 cm^{-1}, 1014 cm^{-1}, 1138 cm^{-1}, and 3390 cm^{-1}), organic molecules (646 cm^{-1}, 760 cm^{-1}, 846 cm^{-1}, 1506 cm^{-1}, 1560 cm^{-1}, 1898 cm^{-1}, 2408 cm^{-1}, 3030 cm^{-1}, 3150 cm^{-1}, and 3280 cm^{-1}), and cyanate compounds (2112 cm^{-1}, 2166 cm^{-1}, and 2284 cm^{-1}). (B) Spectrum from a white crust that formed on an upper wall of the lava tube showing more distinct gypsum signatures (414 cm^{-1}, 486 cm^{-1}, 618 cm^{-1}, 1012 cm^{-1}, 1136 cm^{-1}, 3390 cm^{-1} and 3494 cm^{-1}) with organic molecules (646 cm^{-1}, 760 cm^{-1}, 846 cm^{-1}, 1508 cm^{-1}, 1770 cm^{-1}, 2408 cm^{-1}, 2634 cm^{-1}, and 3148 cm^{-1}), and cyanate compounds (2062 cm^{-1} and 2266 cm^{-1}).

Recurring Raman signatures for cyanates were frequently observed in secondary precipitates dominated by gypsum ~ 2062 cm^{-1}, 2112 cm^{-1}, 2166 cm^{-1}, 2266 cm^{-1}, 2302 cm^{-1}, commonly with (P-H) 2408 cm^{-1}, and (P-H) 2460 cm^{-1} (Fig. 7). It is interesting to note that infrequent phosphatic peaks observed on the lower end of the spectrum (~970 cm^{-1}) in these samples were not observed in the Hveragil samples. Other cyanate-related compounds with the gypsum included (NCS) 944 cm^{-1}, (COCN) 1192 cm^{-1}, (-SC≡N) 2174 cm^{-1}, (P-CN) 2207 cm^{-1}, (-OCN) 2248 cm^{-1}, (-N=C=O) 2284 cm^{-1} in association with biomolecular Raman peaks (C-S-C) 646 cm^{-1}, (NH rocking) 760 cm^{-1}, (C-O-O) 846 cm^{-1}, (NH_3) 1486 cm^{-1}, (C=O) 1749 cm^{-1}, (C=O) 1898 cm^{-1}, (C=C=C)1940–cm^{-1} - 1964 cm^{-1}, (nitrile complex) 2334 cm^{-1}, (OH carboxylic acid) 3148 cm^{-1}, (C-H) 3278 cm^{-1}, and (N-M stretch) 3382 cm^{-1}. In some cases, bands attributed to isothiocyanates were detected in the lower end of the Raman spectrum ~ 919 cm^{-1} along with the other higher-frequency shifts. Also, in contrast with the Hveragil samples in which urea was detected, signatures for urea were not observed in the lava tube samples. Figure 8 shows Raman spectra correlated with possible luminescence features that overlap with the cyanate peaks from a mini-stalactite sample coated in sulfate; similar features were observed with the portable Raman spectrometer, but with lower peak intensity. Raman mapping shows a connection between the organic phosphorous compounds, gypsum, and the cyanates. In contrast with the Hveragil samples, the cyanate signatures occur almost exclusively with multiple organic phosphorous compounds, and the presence of the Raman peak at 2207 cm^{-1} attributed to P-C≡N could be

evidence of biomolecular-cyanate coordination [18]. In addition, the lava tube samples were also analyzed by X-ray Diffraction (XRD), and no phosphate minerals were detected.

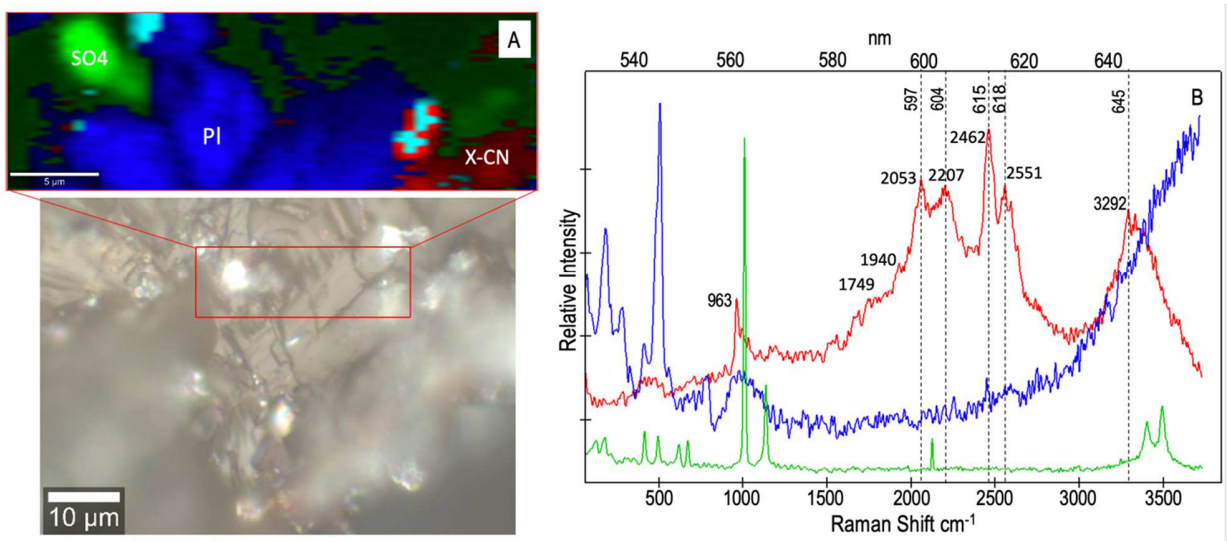

Figure 8. Micro-Raman measurements of mini-stalactite identify potential cyanates and phosphatic compounds with precipitates of gypsum on the plagioclase-rich basalt. (A) 10 µm x 25 µm scan area (red box) and Raman spectra map showing plagioclase (blue, peak position 505 cm^{-1}), gypsum (green, peak position 1014 cm^{-1}), cyanates (red, peak position 2064 cm^{-1}), and phosphatic compounds (teal, peak position 2456 cm^{-1}). (B) Average Raman spectra for each component shown in the map with Raman peak position (bottom axis) against luminescence bands (upper axis, dotted lines), gypsum (green), plagioclase (blue), cyanates and phosphatic compounds (red).

UVN LIBS results from the samples of secondary precipitates showed the expected elemental composition for gypsum and thenardite, with the addition of Sr and P in some of the precipitates (Fig. 9 A,B). The LWIR LIBS spectrum of these samples also showed strong signature emissions of sulfate, water, minor carbonate, and hydrated silicates at 8.7 µm (1149 cm^{-1}), 6.6 µm (1515 cm^{-1}), 6.8 µm (1470 cm^{-1}), and 9.2 µm (1086 cm^{-1}), respectively. As noted with the Raman data, signatures for cyanates occur with the secondary precipitates dominated by gypsum. The bands ascribed to cyanates are observed were observed at (OCN) 6.98 µm (1433 cm^{-1}) and (SCN) 9.05 (1105 cm^{-1}) µm. The CN stretching bands attributed to either chlorophyll, amino acids, or cyanates were observed at 6.23 µm (1605 cm^{-1}), 8.57 µm (1166 cm^{-1}), 9.35 µm (1069 cm^{-1}), and 9.53 µm (1049 cm^{-1}). The NH bending bands observed at 6.55 µm (1525 cm^{-1}) could be attributed to amino acid or cyanates. Other types of organic compounds were also observed by bands: C=O stretching at 5.78 µm (1730 cm^{-1}) and 5.9 µm (1695 cm^{-1}), CH bending at 6.76 µm (1479 cm^{-1}), 7.21 µm (1386 cm^{-1}), and 9.23 µm (1083 cm^{-1}), C-O stretching at 8.76 µm and 9.44 µm (1141 and 1059 cm^{-1}) and C-C stretching at 9.86 µm (1014 cm^{-1}) In a depth profiling study, the LWIR LIBS spectra of each of the two consecutive laser pulses fired on the same sample surface location are shown in Fig. 9D. Depth profiling through the white coating (first shot spectrum in Figure 9D) on a stalactite sample shows sulfate, organics, and cyanate signatures in the coating, while the basalt ~ 3.5 µm beneath shows a silicate with similar organics and weaker cyanate signatures (second shot spectrum in Fig 9D).

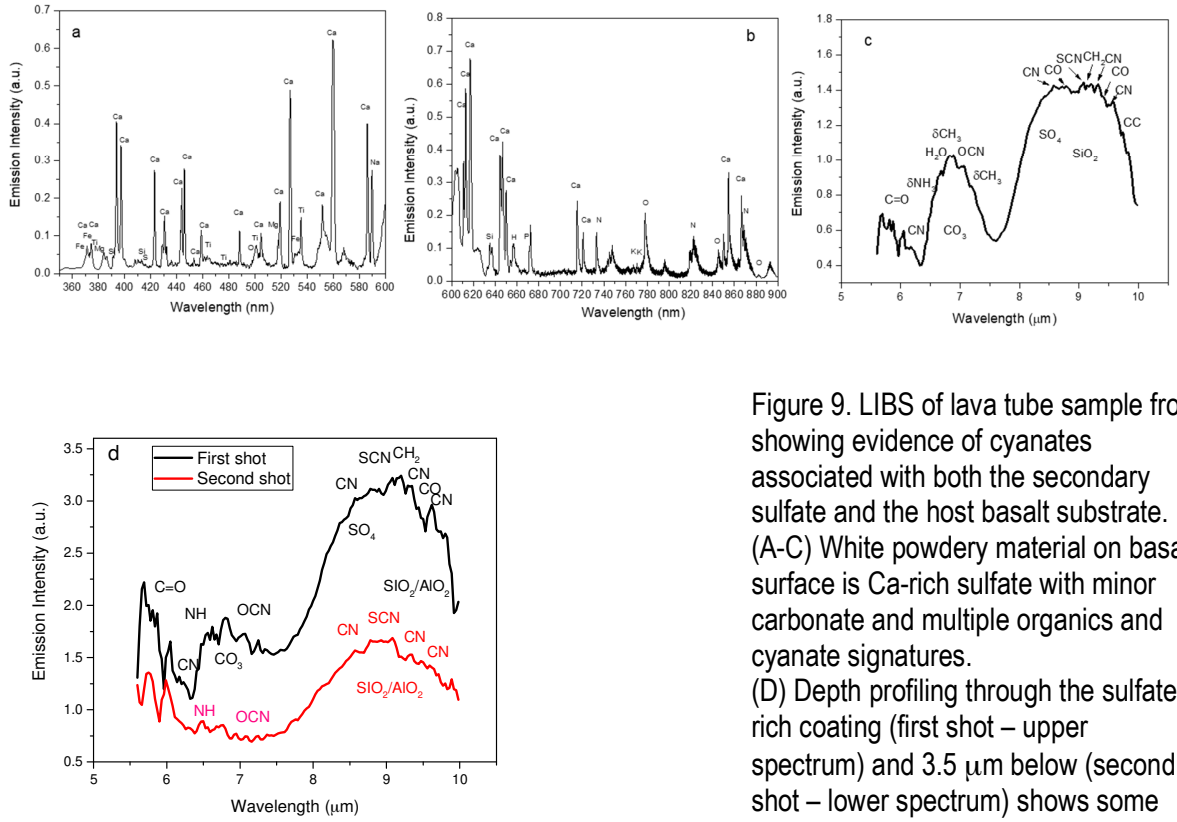

Figure 9. LIBS of lava tube sample from showing evidence of cyanates associated with both the secondary sulfate and the host basalt substrate. (A-C) White powdery material on basalt surface is Ca-rich sulfate with minor carbonate and multiple organics and cyanate signatures. (D) Depth profiling through the sulfate-rich coating (first shot – upper spectrum) and 3.5 μm below (second shot – lower spectrum) shows some differences in composition.

Aside from being underground, a distinct difference in the environment of the Mauna Loa lava tube compared to that of Hveragil is that mosses and lichen are rare around the lava tube, and microbial mats are only observed near skylights or the entrance of the lava tube. This lack of biodiversity may be the main reason for the limited distribution of biomolecular signatures observed by Raman and LIBS in the lava tube in comparison to the wide variety seen at Hveragil. Alternatively, this could be an example of the limits of targeted vs bulk sample measurements. The GC-MS data obtained after the 200-600°C pyrolysis temperature range indicated a high diversity and number of organic molecules in the samples studied. The most abundant chemical families included hydrocarbons, polycyclic aromatic hydrocarbons, nitrogen-, and oxygen bearing organics. Minor amounts of phosphorus-, chlorine-, and sulfur-bearing organics were detected as well. The nitrogen-bearing species represented more than a quarter of the total number of compounds detected and included branched and/or aromatic nitriles (e.g., methyl-propanenitrile, benzonitriles), amines (e.g., trimethylamine, propyl-benzenamine), pyrroles and indoles (e.g., pyrrole, methyl-indole), and pyridines. A number of polar compounds including C_8, C_9, C_{10}, C_{11}, C_{12}, C_{14}, C_{16} and C_{18} fatty acids, one amino acid (proline) and a potential nucleobase (cytosine) were also detected (Fig. 10). Like the Hveragil sample, long-chain alkanes were still present in the chromatogram obtained after derivatization (Fig. 6).

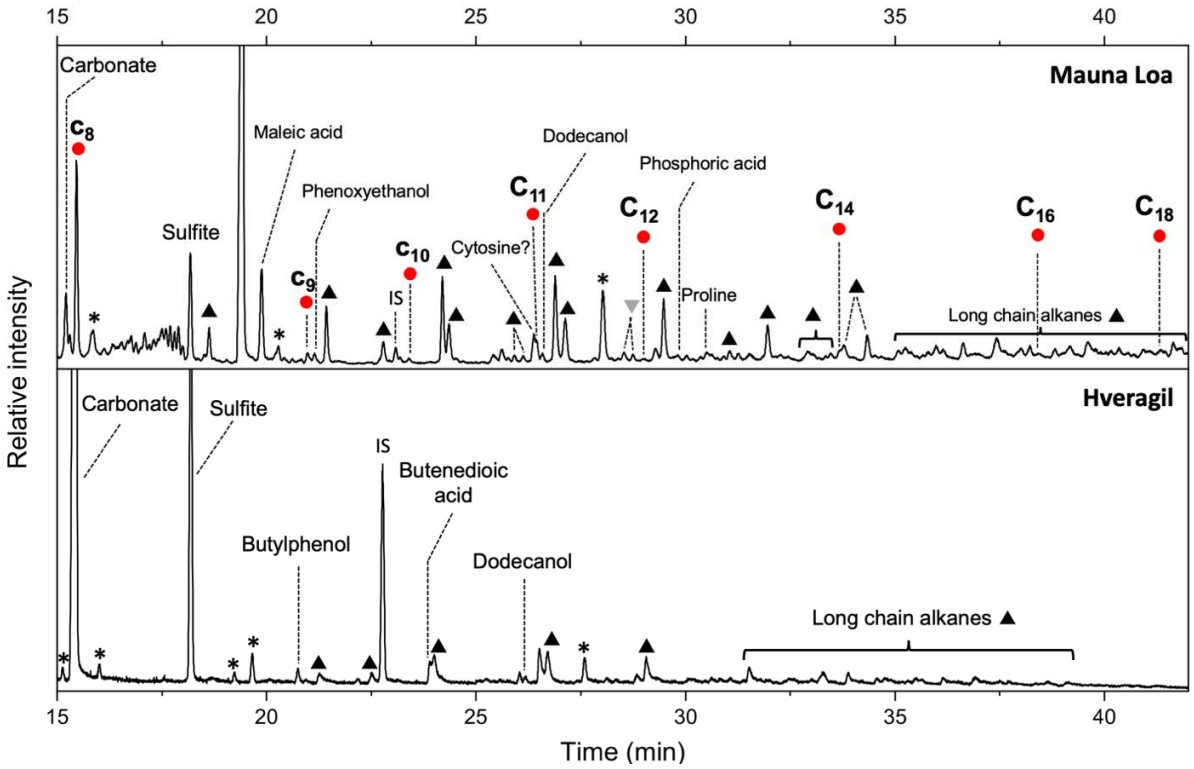

Figure 10. Portion of the extracted m/z 57 ion chromatograms obtained from the pyrolysis coupled to MTBSTFA-DMF derivatization of a Mauna Loa (top) and Hveragil (bottom) sample displaying the detection of C_8-C_{18} fatty acids (red dots), alkanes (black pointing up triangles), alkenes (gray pointing down triangles), other (di)carboxylic acids, alcohols, proline, and potentially cytosine. Carbonate and sulfite were also detected in their derivatized forms. 3-fluorovaline was used as internal standard (IS) in order to ensure the efficiency of the derivatization reaction. *Peaks indicate common MTBSTFA-DMF byproducts.

The broad array of sulfur-bearing organic compounds detected at higher temperatures after the pyrolysis GC-MS are consistent with the thermal breakdown of the sulfate minerals. The biomolecules detected are also consistent with the Raman data, and suggest the presence of extant life and active metabolism in the samples. In an oxic environment, however, it is a mystery if or how the microbes are utilizing the sulfate. We expect sulfate metabolisms in anaerobic environments, but the lava tube is an open environment not limited by oxygen. In a parallel study of the same lava tube, the taxanomic makeup of the microbial communities was examined using 16s SSU rRNA sequencing and whole genome shotgun sequencing [53]. Interestingly, despite the predominance of sulfates, the majority of identified metabolisms were unrelated to sulfur. Even more interesting, the lava tube contained large amounts of unclassified taxa. Previous studies on the biogeochemical dynamics of lava tubes have shown that the cave waters largely contribute to the initial formation of secondary cave minerals, and during dry periods microbes take over to affect the formation of observed speleotherms (e.g., mini stalactites) and to mobilize cave water components, but there is much that is still unknown [4, 54]. Further studies focusing on cyanate metabolisms and elemental distributions should reveal more about the connection between microbes and these secondary formations.

Much like the post-colonization of microbes on the carbonates at Hveragil, here too, it seems likely that the microbes were not directly responsible for the precipitation of the sulfates. In most cases, sulfates were observed in locations in the lava tube where water was either actively dripping or present as a thin layer on the basalt surface, suggesting the waters percolating through the basalts play a large role in the sulfate formation [55]. The source of the water in the tube is rain that seeps down through the lava at the surface, and elements are scavenged from the basalts leading to the precipitation of the secondary minerals as the water percolates through [56]. The water chemistry data showed statistically significant variations between the two main lava tube sections, and the waters throughout the tube were pH 7.5 regardless of location. Ca was the most abundant element in the tube waters, which correlates well with the prevalence of Ca-sulfate minerals. The abundance of Na also correlates well with the presence of the Na-sulfates that formed the second most prevalent precipitate on the lava tube rocks that we measured. Na concentrations were high regardless of tube location.

Of the minor elements measured in the water samples, Cu and Mn seem to be present in higher concentrations in the tube section nearest the entrance, and As seems to be absent from the more isolated tube section. Despite the relatively high concentrations of Mg, Ba, and V in the cave waters, we did not detect any related minerals with Raman or LIBS spectroscopy. Both Ba- and Mg-sulfates have very distinct Raman signatures, but it is possible that these elements were present but not integrated within the mineral lattice [57]. Hawaiian basalts in general can contain up to of the several hundred ppm of V, and vanadium-chloride complexes are known to form as blue-green precipitates under fumarolic conditions in other types of lava tubes but were not observed in our lava tube [56]. Further mineral and elemental studies utilizing thin sections of these samples will shed light on how these water-derived elements are incorporated and/or how the microbes may be involved.

Both isothiocyanate and thiocyanate were detected in the basalt and secondary sulfates in the lava tube with Raman spectroscopy and LIBS. Mauna Loa is an active volcano, and the sulfur in the system may be derived from S-bearing volcanic aerosols that periodically permeate the tube. This may also be a source of the cyanates detected, particularly the thiocyanates, involving reactions between volcanically-derived CN^- and sulfur [58]. Some of the other water components, such as Cu may have also contributed to the formation of the thiocyanates. Thiocyanates have been formed in laboratory studies using Cu at room temperature under air in the presence of sulfides or CN^- [59]. The oxidation of thiocyanates in the presence of iron and water results in the formation of sulfate as well [60] (Sharma 2003). Given the scope of this study and the ephemeral nature of both the cyanates and sulfate minerals in the lava tube, it is not possible to assess the exact mechanisms for cyanate-sulfate chemistry in this system. In addition, direct measurements of volcanic aerosols have not been made, and neither native sulfur nor sulfides were detected in the lava tube samples.

In the sulfur-cyanate system, HCO_3, NH_4, and SO_4 are byproducts of thiocyanate hydrolysis [11]. NH_4, was only marginally present in the sulfate coatings on the mini-stalactites, and we did not observe HCO_3 in our samples. In the few instances where we detected a calcium carbonate with the gypsum, there were no co-occurring cyanate signatures. Instead, the cyanate signatures seem to be coupled with carbon-rich and phosphorous compounds. And, intriguingly, the GC-MS data showed a high yield of organic compounds associated with the sulfate samples with

carbonate, so there does seem to be some correlation between the carbonate precipitates and microbial activity, but a clear link to cyanates is not possible based on our results so far.

Conclusions

One of the goals of this work was to inform the spectroscopic detection of nitrogen compounds such as cyanates in basaltic planetary analog environments using a mission-relevant approach of limited sample measurements of intact samples with mission-relevant techniques to understand their potential as biosignatures. For any landed mission with constrained access to target materials, discerning signatures of life and habitability can be daunting, particularly where the preservation of organic compounds that contain the building blocks of life is limited. The Raman spectroscopic signatures for cyanates fell within a range (~2000 cm^{-1} – 2200 cm^{-1}) that was distinguishable from other compounds and minerals that occurred with them. This spectral range is often overcome by luminescence artifacts that can be both useful as indicators of REE or metal chemistry and at the same time detrimental to identifying key Raman signatures for cyanates and related compounds. The complexity of natural samples and potential abiotic origins of some of the cyanate compounds forced us to also rely on spectral signatures for bio-related byproducts (e.g., NH_4, urea) that occured in the "fingerprint region". and overlapped with those of minerals and other organic molecules, making our interpretation of the sources and pathways of the cyanates difficult. The additional information provided by the LIBS, ICP-MS, and GC-MS data was helpful, but a higher level of detailed analyses was needed for clarification of some of these potential pathways.

The rocks at Hveragil are considered to be potential analogs for the olivine-associated carbonates detected in the NE Syrtis region of Mars [61, 62]. The subsurface environment in the Mauna Loa lava tube is an analog for martian lava tubes, where life may potentially exist within the protective environment underground [5]. A better understanding of how to detect spectroscopic signatures of bioalteration in the rocks studied will benefit the current NASA Perserverance rover mission on Mars and upcoming missions there and to other rocky planetary bodies. The role of cyanates in the biotic nitrogen cycle has been well-studied in marine systems and in terrestrial soils, but little is known about volcanic systems [9, 10] . Further studies of these and other volcanic environments will shed light on the pathways that form cyanates, their role in biotic nitrogen cycling, and their relationships to secondary mineral formation. Once these pathways and relationships are better established for the systems presented, cyanates may yet prove to be useful biosignatures for planetary exploration.

Acknowledgements

We wish to thank the National Aeronautics and Space Administration (NASA) for support under award number a cooperative agreement between the Department of Astronomy, University of Maryland, College Park, and NASA Goddard Space Flight Center, and for providing funds through the Internal Scientist Funding Model program Fundamental Laboratory Research (FLaRe), the Instrument Concepts for Europa Exploration (ICEE-2013) Program for Research Opportunities in Space and Earth Sciences. We would also like to thank the Internal Scientist Funding Model (ISFM) Goddard Instrument Field Team (GIFT) for providing the infrastructure and support to do our fieldwork. S. S. Johnson and M. Millan would like to acknowledge the

"Using Organic Molecule Detections in Mars Analog Environments to Interpret the Results of the SAM Investigation on the Mars Science Laboratory Mission" NASA-GSFC grant (NNX17AJ68G). Special thanks to Jose Aponte for providing CN reference standards.

References

1. Peterson, D.W., et al., *Development of lava tubes in the light of observations at Mauna Ulu, Kilauea Volcano, Hawaii.* Bulletin of Volcanology, 1994. **56**: p. 343-360.
2. Greeley, R., *The role of lava tubes in Hawaiian volcanoes.* USGS Professional Paper, 1987. **2**: p. 1589-1601.
3. Kulkarni, H.V., et al., *Geochemical interations among ater, minerals, microbes, and organic matter in formation of speleotherms in volcanic (lava tube) caves.* Chemical Geology, 2022. **594**(120759).
4. Northrup, D.E., et al., *Lava and cave microbial communities withn mats and secondary mineral deposits: implications for life detection on other planets.* Astrobiology, 2011. **11**(7): p. 601-618.
5. Leveille, R.J. and S. Datta, *Lava tubes and basaltic caves as astrobiological targets on Earth and Mars: A review.* Planetary and Space Science, 2010. **58**: p. 592-598.
6. Bower, D.M., et al., *Spectroscopic characterization of samples from different environments in a volcano-glacial region in Iceland: implications for in situ planetary exploration.* Spectrochimica Acta Part A, 2021. **263**(120205): p. 1-14.
7. Cousins, C., *Volcanogenic fluvial-lacustrine environments in Iceland and their utility for identifying past habitability on Mars.* Life, 2015. **5**: p. 568-586.
8. Chan, M., et al., *Deciphering biosignatures in planetary contexts.* Astrobiology, 2019. **19**(9): p. 1-28.
9. Mooshamer, M., et al., *Cyanate is a low abundance but actively cycled nitrogen compound in soil.* Communications Earth & Environment, 2021. **2**(161): p. 1-10.
10. Widner, B. and M.R. Mulholland, *Cyanate distribution and uptake in north Atlantic coastal waters.* Limnology and Oceanography, 2017. **62**: p. 2538-2549.
11. Ni, G., et al., *Microbial community and metabolic activity in thiocyanate degrading low temperature microbial fuel cells.* Frontiers in Microbiology, 2018. **9**: p. 1-10.
12. Wen, N. and M.H. Brooker, *Rate constants for cyanate hydrolysis to urea: a Raman study.* Canadian Journal of Chemistry, 1994. **72**: p. 1099-1106.
13. Czamara, K., et al., *Raman spectroscopy of lipids: a review*. Journal of Raman Spectroscopy, 2014. **46**: p. 4-20.
14. Jehlicka, J., H.G.M. Edwards, and A. Oren, *Raman spectroscopy of microbial pigments.* Applied and Environmental Microbiology, 2014. **80**(11): p. 3286-3295.
15. Dufresne, W.J.B., C.J. Rufledt, and C.P. Marshall, *Raman spectroscopy of the eight natural carbonate minerals of calcite structure.* Journal of Raman Spectroscopy, 2018. **49**: p. 1999-2007.
16. Mabrouk, K.B., et al., *Raman study of cation effect on sulfate vibration modes in solid state and in aqueous solutions.* Journal of Raman Spectroscopy, 2013. **44**(11): p. 1603-1608.

17. Edwards, H.G.M., et al., *Biomarkers and their Raman spectroscopic signatures: a spectral challenge for analytical astrobiology.* Phil. Trans. R. Soc. A, 2014. **372**: p. 1-12.
18. Socrates, G., *Infrared and Raman characteristic group frequencies*. 3 ed, ed. G. Socrates. 2001, West Sussex, england: John Wiley & Sons, Ltd.
19. Olafsson, M., H. Torfason, and K. Gronvold. *Surface exploration and monitoring of geothermal activity in the Kverkfjoll geothermal area, central Iceland*. in *Proceedings World Geothermal Congress*. 2000. Kyushu-Tohoku, Hapan: International Geothermal Association.
20. Cousins, C.R., et al., *Glaciovolcanic hydrothermal environments in Iceland and implications for their detection on Mars.* Journal of Volcanology and Geothermal Research, 2013. **256**: p. 61-77.
21. Nakamoto, K., *Infrared and Raman Spectra of Inorganic and Coordination Compounds Part B: Applications in Coordination, Organometallic, and Bioinorganic Chemsitry*. 6th ed, ed. K. Nakamoto. 2009, New Jersey: Wiley. 417.
22. Yang, C.S.-C., et al., *Long-Wave Infrared (LWIR) Molecular Laser-Induced Breakdown Spectroscopy (LIBS) Emissions of Thin Solid Explosive Powder Films Deposited on Aluminum Substrates.* Applied Spectroscopy, 2017. **71**(4): p. 1-7.
23. Mahaffy, P., et al., *The Sample Analysis at Mars investigation and instrument suite.* Space Science Reviews, 2012. **170**: p. 401-478.
24. Bersani, D., et al., *Plagioclase composition by Raman spectroscopy.* Journal of Raman Spectroscopy, 2018. **49**: p. 684-698.
25. Edwards, H.G.M., E.M. Newton, and D.D. Wynn-Williams, *Molecular structural studies of lichen substances II: atranorin, gyrophoric acid, fumarprotocetraric acids, rhizocarpic acids, calcyin, pulvinic dilactone and usnic acid.* Journal of Molecular Structure, 2003. **651-653**: p. 27-37.
26. Frost, R.L., et al., *Raman spectroscopy of urea and urea-intercalated kaolinites.* Spectrochimica Acta Part A, 2000. **56**(56): p. 1681-1691.
27. Chapados, C., S. Lemieux, and R. Carpentier, *Protein and chlorophyll in photosystem II probed by infrared spectroscopy.* Biophysical Chemistry, 1991. **39**(3): p. 225-239.
28. Terpugov, E.L., O.V. Degtyareva, and V.V. Savransky, *Fourier Transform Infrared Spectroscopy Analysis of Pigments in Fresh Tobacco Leaves.* Physics of Wave Phenomena, 2019. **27**(1): p. 13-19.
29. Barth, A., *Infrared spectroscopy of proteins.* Biochimica Biophysica Acta, 2007. **1767**(9): p. 1073-1101.
30. Hirschmann, R.P., R.N. Kniseley, and V.A. Fassel, *Infrared spectroscopy of proteins.* Biochimica Biophysica Acta, 2007. **1767**(9): p. 1073-1101.
31. Miller, F.A. and W.B. White, *Infrared and Raman spectra of methyl thiocyanate.* Advances in Molecular Spectroscopy, 1962(875-884).
32. Munoz-Iglesias, V., et al., *Raman spectroscopic peculiarities of Icelandic poorly crystalline minerals and their implications for Mars exploration.* Scientific Reports, 2022. **12**.
33. Tomic, Z., P. Makreski, and B. Gajic, *Identification and spectra-structure determination of soil minerals: Raman study supported by IR spectroscopy and X-ray powder diffraction.* Journal of Raman Spectroscopy, 2010. **41**: p. 582-586.
34. Lane, M.D. and P.R. Christensen, *Thermal infrared emission spectroscopy of anhydrous carbonates.* Journal of Geophysical Research, 1997. **102**: p. 25581-25592.

35. Barazorda-Ccahuana, H.L., et al., *Vibrational analysis of manganese (II) oxalates hydrates: an in silico statistical approach.* ACS Omega, 2020. **5**: p. 9071-9077.
36. Miralles, I., et al., *Lichens around the world: a comprehensive study of lichen survival biostrategies detected by Raman spectroscopy.* Analytical Methods, 2015. **7**: p. 6856-6868.
37. Degen, I.A. and G.A. Newman, *Raman spectra of inorganic ions.* Spectrochimica Acta 1993. **49A**(5/6): p. 859-887.
38. Bernardini, S., et al., *Raman spectra of natural manganese oxides.* Journal of Raman Spectroscopy, 2019. **50**: p. 873-888.
39. Douglas, G.R., *Manganese-rich rock coatings from Iceland.* Earth Surface Processes and Landforms, 1987. **12**: p. 301- 310.
40. Moroz, T.N., H.G.M. Edwards, and S.M. Zhmodik, *Detection of carbonate, phosphate minerals and cyanobacteria in rock from the Tomtor deposit, Russia, by Raman spectroscopy.* Spectrochimica Acta Part A, 2021. **250**: p. 1-6.
41. Lenz, C., et al., *Laser-induced REE3+ photoluminescence of selected accessory minerals - an advantageous artefact in Raman spectroscopy.* Chemical Geology, 2015. **415**: p. 1-16.
42. Berben, T., et al., *Analysis of the genes involved in thiocyanate oxidation during growth in continuous culture of the haloalkaphilic sulfur-oxidizing bacterium Thioalkalivibrio thiocyanoxidans ARh 2T using transcriptomics.* Molecular Biology and Physiology, 2017. **2**(6): p. 1-12.
43. Dorn, R.I. and T.M. O'berlander, *Rock varnish.* Progress in Physical Geography: Earth and Environment, 1982. **6**(3): p. 317-367.
44. Krumbein, W.E. and K. Jens, *Biogenic varnishes of the Negev Desert (Israel): an ecological study of iron and manganese transformation by cyanobacteria and fungi.* Oceologia, 1981. **50**: p. 25-38.
45. Wang, A., et al., *Raman imaging of extraterrestrial materials.* Planetary and Space Science, 2015. **112**: p. 23-34.
46. Bower, D.M., et al., *Micro Raman imaging of planetary analogs: nanoscale characterization of past and current processes*, in *Spectroscopy and Characterization of Nanomaterials and Novel Materials. Experiments, Modeling, Simulations, and Applications*, P. Misra, Editor. 2022, Wiley: Berlin. p. 417-452.
47. Fujita, Y., et al., *Stimulation of microbial urea hydrolysis in groundwater to enhance calcite precipitation.* Environmental Science & Technology, 2008. **42**: p. 3025-3032.
48. Ma, L., et al., *Beneficial factors for biomineralization by ureolytic bacterium Sporosarcina pasteurii.* Microbial Cell Factories, 2020. **19**(12): p. 1-12.
49. Malhotra, H., S. Kaur, and P.S. Phale, *Conserved metabolic and evolutionary themes in microbial degradation of carbamate pesticides.* Frontiers in Microbiology, 2021. **12**: p. 1-31.
50. Mathewman, R., Z. Martins, and M.A. Sephton, *Type IV kerogens as analogues for organic macromolecular materials in aqueously altered carbonaceous chondrites.* Astrobiology, 2013. **13**(4): p. 324-333.
51. Sawlowicz, Z., *A short review of pyroproducts (lava tubes).* Annales Societatis Geologorum Poloniae, 2021. **90**: p. 513-534.
52. Prieto-Taboada, N., et al., *Raman spectra of the different phases in the CaSO4-H2O system.* Analytical Chemistry, 2014. **86**: p. 10131-10137.

53. Fishman, C.B., et al., *Extreme niche partitioning and microbial dark matter in a Mauna Loa lava tube.* Journal of Geophysical Research: Planets, Accepted: p. 1-44.
54. Prescott, R.D., et al., *Islands within islands: bacterial phylogenetic structure and consortia in Hawaiian lava caves and fumaroles.* Frontiers in Microbiology, 2022. **13**: p. 1-20.
55. Forti, P., *genetic processes of cave minerals in volcanic environments: an overview.* Journal of Cave and Karst Studies, 2005. **67**(1): p. 3-13.
56. White, W.B., *Secondary minerals in volcanic caves: data from Hawai'i.* Journal of Cave and Karst Studies, 2009. **72**: p. 75-85.
57. Bower, D.M., et al., *The co-evolution of Fe,-Ti,-oxides and other microbially induced mineral precipitates in sandy sediments: understanding the role of cyanobacteria in weathering and early diagenesis.* Journal of Sedimentary Research, 2015. **85**: p. 1213-1227.
58. Kurashova, I. and A. Kamyshny, *Kinetics of thiocyanate formation by reaction of cyanide and its iron complexes with thiosulfate.* Aquatic Geochemistry, 2019. **25**: p. 219-236.
59. Castanheiro, T., et al., *Practical access to aromatic thiocyanates by CuCN-mediated direct aerobic oxidative cyanation of thiophenols and diaryl disulfides.* European Journal of Organic Chemistry, 2014: p. 7814-7817.
60. Sharma, V.K., *Destruction of cyanide and thiocyanate by ferrate [Iron(VI)].* The European Journal of Mineral Processing and Environmental Protection, 2003. **3**(3): p. 301-308.
61. Goudge, T.A., et al., *Assessing the mineralogy of th watershed and fan deposits of the Jezero crater paleolake system, Mars.* Journal of Geophysical Research: Planets, 2015. **120**: p. 775-808.
62. Ehlmann, B.L. and J.F. Mustard, *An in-situ record of major environmental transitions on early Mars at Northeast Syrtis Major* Geophysical Research Letters, 2012. **39**: p. 1-7.